Molecular dynamics simulation and experimental validation of nanoscale droplet wetting and anti-icing performance on OTS selfassembled monolayers

Junwei Qin, Wenrui Wang, Shuming Du, Bochong Liu, Lu Xie, Pascal Brault

Molecular dynamics simulation and experimental validation of nanoscale droplet wetting and anti-icing performance on OTS self-assembled monolayers

Junwei Qin[a], Wenrui Wang[a*], Shuming Du[b], Bochong Liu[a], Lu Xie[a], Pascal Brault[c*]

a) School of Mechanical Engineering, University of Science and Technology Beijing, Beijing 100083, China

b) Beijing Key Laboratory of Power Generation System Functional Material, National New Energy Technology Research Institute Ltd, Beijing 102209, China

c) Universit´e d'Orl´eans, GREMI, UMR 7344, CNRS, Orl´eans 45067, France

* Corresponding author: gmbitwrw@ustb.edu.cn (W. Wang). and pascal.brault@univ-orleans.fr (Pascal Brault)

Abstract

This study explores the performance of octadecyltrichlorosilane (OTS) self-assembled monolayer (SAM) coatings on SiO_2 substrates through molecular dynamics (MD) simulations and experimental validations. MD simulations at 300 K investigated the molecular packing, wettability, and droplet dynamics of OTS SAMs across varying coverage densities (0.18 to 3.48 molecules nm^{-2}). Results indicate that monolayer thickness increases from 0.3 nm to 2.4 nm with coverage density, while contact angles rise from 0° to 132.7°, with a peak at 125.2° due to surface roughness of 0.262 nm at 1.80 molecules nm^{-2}. Rolling friction decreases as droplet velocity rises from 4.894 m/s to 41.291 m/s, and self-driven droplet jumping at medium and high coverage enhances self-cleaning. Experimentally, OTS-coated wind turbine blade composite samples delayed icing to 649 s and complete icing to 725 s at -10°C, compared to 12 s and 17 s for SiO_2 hydrophilic coatings, and 92 s and 121 s for uncoated surfaces, attributed to reduced contact area and low surface energy. De-icing tests showed OTS coatings achieve ice detachment in 58 s on tilted surfaces via a lubricating water layer, despite longer melting times of 215 s on horizontal surfaces. These findings highlight OTS SAMs' superior hydrophobicity, low friction, and anti-icing/de-icing performance, offering potential for high-altitude engineering applications.

Keywords: Octadecyltrichlorosilane, Self-assembled monolayer, Molecular dynamics simulation, Anti-icing coating, Wetting behavior

Introduction

Self-assembled monolayers (SAMs) have been extensively utilized for surface modification of substrates due to their well-defined microstructures and wetting behaviors, which closely resemble those of practical coatings. Pioneering work by Bigelow et al.[1] in 1940 first reported the formation of SAMs on substrates, where molecules covalently bond to suitable surfaces, enabling the creation of densely packed and robust monolayer films. Silane-based SAMs, in particular, exhibit broad applicability across diverse substrates such as silicon[2], glass[3], metals[4], mica[5], and polydimethylsiloxane (PDMS)[6]. The wettability of these surfaces can be tailored between hydrophobic and hydrophilic states by selecting silanes with specific terminal functional groups. For instance, grafting hydrophobic silane SAMs (e.g., methyl-terminated) onto hydrophilic silicon oxide surfaces yields water contact angles exceeding 100°[7], while also demonstrating exceptional thermal stability up to 250°C[7, 8]. This hydrophobization process significantly reduces surface tension, imparting self-cleaning properties[9] and enabling applications in protein/bacterial adsorption studies[10], polymer dewetting[11], and selective-area atomic layer deposition[12].

Trichlorosilane derivatives[13, 14] and phosphate derivatives[15] can both be grafted onto hydroxylated silica surfaces, forming chemically bonded semicrystalline two-dimensional films that are fundamentally SAMs. Among these, octadecyltrichlorosilane (OTS) stands out as a widely used organosilane derivative, capable of modifying the surface properties of solid substrates through the formation of compact, highly oriented SAMs[16]. Lessel et al.[2] developed a wet chemical protocol for

grafting methyl-terminated molecules (e.g., dodecyltrichlorosilane and OTS) onto silicon wafers. While their work provided critical insights into the surface parameters of silane SAMs, the precise molecular arrangement of silane molecules on substrates remains unresolved. Gutfreund et al.[17] proposed a molecular packing model for alkylsilanes using X-ray scattering, revealing that the actual thickness of silane layers is smaller than their theoretical molecular length, with alkyl chains adopting a tilted orientation on the substrate. However, X-ray scattering primarily measures electron density and lacks direct resolution of molecular-scale arrangements. The nanoscale geometric features of silane SAMs dictate their macroscopic properties, yet despite extensive experimental characterization of surface energy, roughness, and layer thickness[2, 7, 8, 18], a molecular-level understanding of alkylsilane SAMs remains elusive.

Molecular dynamics (MD) and quantum chemical simulations have emerged as powerful tools for probing SAM properties at the molecular scale. Zhang et al.[19] combined density functional theory (DFT) and MD simulations to identify the optimal packing structure of OTS SAMs on silica, demonstrating that intermediate packing densities minimize system energy. Zhan et al.[20] performed MD simulations of hydroxylated alkylsilane SAMs on planar silicon substrates, revealing that molecular tilt angles depend on surface coverage and specific molecular packing configurations. Barlow et al.[21] observed that OTS layers near silica substrates exhibit a crystalline yet disordered structure akin to a fluid phase. Barriga et al.[22] further employing MD simulations, investigated the effects of molecular orientation and temperature on OTS SAMs, finding that tightly packed OTS molecules adopt near-vertical orientations.

While varying packing arrangements led to significant energy differences, the final tilt angle remained temperature-independent.

The tribological and wetting properties of alkylsilane SAMs on silicon are of particular relevance to micro/nanoelectromechanical systems (MEMS/NEMS), where cooling efficiency is closely tied to the wetting behavior of micro/nanoscale droplets[23]. Chandross et al.[24] analyzed the impact of molecular disorder on the frictional properties of alkylsilane SAMs, noting that stick-slip phenomena vanish at maximal disordered monolayer coverage. Pastorino et al.[25] modeled shear forces between silane SAMs using a bead-spring polymer fluid model, observing fluid-like layering and molecular alignment along the shear direction. Li et al.[26] demonstrated via MD simulations that two distinct SAMs (HSAM and FSAM) achieve superlubricity on graphite in aqueous environments, mediated by a continuous interfacial water film. Additionally, Cione et al.[4] investigated ionic liquid wetting on gold and silica substrates functionalized with alkylthiol and alkylsilane monolayers, showing that hydroxyl-terminated surfaces reduce ion-ion attraction and lower local surface tension.

Despite significant progress in employing molecular dynamics (MD) and quantum chemical methods to investigate the microscopic properties of silane SAMs, several limitations persist. First, most studies rely on idealized models that often neglect complex real-world factors, such as surface defects and interfacial chemistry, which can profoundly influence the molecular arrangement and properties of silane layers in practical applications. Additionally, investigations into the dynamic behavior of silane molecules under varying coverage densities and temperature conditions remain limited,

particularly in accurately correlating computational predictions with experimental observations. Second, existing research predominantly focuses on static properties, such as molecular arrangement and layer thickness, while dynamic wetting behaviors, especially the interactions between microscale droplets and surfaces have received insufficient attention. Consequently, there is a pressing need for comprehensive studies that integrate simulations with experimental validations across a broader range of parameters to fully elucidate the behavior of silane SAMs.

This study investigates the wetting properties of OTS SAMs on SiO_2 substrates at 300 K using MD simulations. The molecular packing of alkylsilanes within the SAM was analyzed by systematically varying coverage density, exploring relationships among layer thickness, tilt angle, and surface coverage. The wetting behavior of nanoscale water droplets was examined, focusing on rolling friction and the microscopic mechanisms of droplet jumping at high coverage density. Experimentally, OTS-coated samples, prepared on wind turbine blade composite surfaces, were compared with hydrophilic SiO_2-coated and uncoated samples in icing and de-icing tests. These experiments confirm the superior hydrophobicity, low friction, and anti-icing performance of OTS coatings, driven by enhanced self-cleaning capabilities. The findings highlight potential applications for anti-icing coatings in high-altitude engineering equipment.

Simulation and experimental methods

System setup

The grafting process of OTS SAMs onto hydroxylated SiO_2 surfaces is shown in

Fig. 1a. An initial microscopic configuration, comprising a nanoscale water droplet, grafted OTS molecules, and a SiO_2 substrate, was constructed, as depicted in Fig. 1b. The droplet's center of mass distance from the substrate surface was set to 3.4 nm. The simulation box measured 12.1 × 12.4 × 20 nm^3, with the droplet containing 3764 water molecules. OTS molecule density varied from 0 to 3.48 molecules nm^{-2}[27, 28], with counts and coverage density detailed in Table 1. The substrate was modeled using the α-quartz surface, exhibiting a contact angle of 0°, consistent with experimental measurements of amorphous silica[29]. This high agreement with experimental results stems from the hydroxylation of the substrate surface, where each exposed Si atom is grafted with an OH group (coverage density of 3.48 molecules nm^{-2}), as per Emami et al.[30]. The modeling approach followed methods similar to those reported by Castillo et al.[31] and Summer et al.[32] for constructing OTS SAMs on SiO_2 substrates. Specifically, an OH group was removed from the SiO_2 substrate, and a hydrogen atom was removed from a hydroxylated OTS chain. The unpaired O atom in the OTS molecule was then bonded to the unpaired Si atom in the SiO_2 substrate, with charge balancing applied to ensure the system's net charge remained zero.

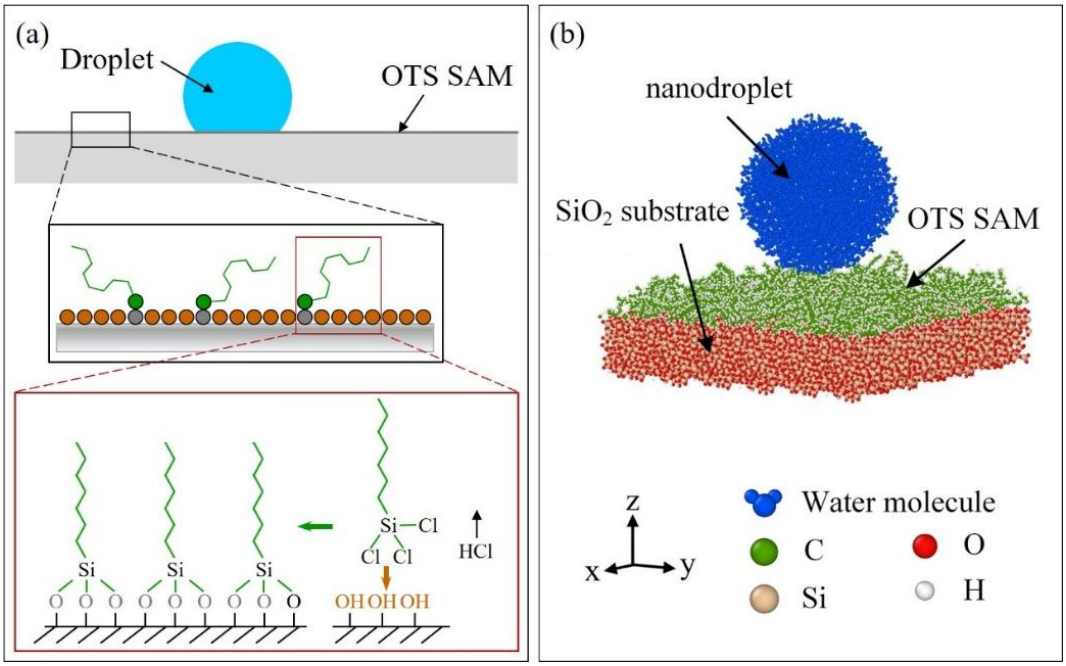

Fig. 1. (a) Grafting process of OTS SAM on hydroxylated SiO_2 surface; (b) Initial wetting model configuration at 1.50 molecules nm^{-2}.

Table 1 OTS molecule counts and corresponding coverage densities in the initial model

OTS Molecule Count	Coverage Density (molecules nm^{-2})	OTS Molecule Count	Coverage Density (molecules nm^{-2})
0	0.00	30	1.80
3	0.18	36	2.16
5	0.30	42	2.51
15	0.90	50	2.99
25	1.50	58	3.48

Potential models

Water molecules were modeled using the SPC/E rigid-body potential, a widely validated model that efficiently captures essential physical properties such as wetting behavior and contact angles, ensuring computational feasibility within the study's scope[33, 34]. Interactions between SiO_2 substrate atoms and OTS molecules were

described using the 12-6 Lennard-Jones (LJ) potential[30], while dihedral parameters for OTS molecules were based on the OPLS all-atom force field[35]. Non-bonded interaction parameters are listed in Table 2. For atoms separated by three bonds, interactions were scaled by a factor of 0.5, and only interactions involving three or more bonds were considered. The 12-6 LJ parameters for interactions between different atom types were calculated using the geometric mixing rule[35], as shown in Eqs. (1) and (2):

$$\sigma_{ij} = \sqrt{\sigma_{ii}\sigma_{jj}} \tag{1}$$

$$\varepsilon_{ij} = \sqrt{\varepsilon_{ii}\varepsilon_{jj}} \tag{2}$$

Table 2 Non-bonded interaction parameters

Atom Type	σ (Å)	ε (kcal/mol)	q (e^-)
C, CH_3	3.500	0.066	-0.180
C, CH_2	3.500	0.066	-0.120
H, CH	2.500	0.030	0.060
O	3.154	0.152	-0.510
H, OH	2.352	0.219	0.225
Si	3.920	0.600	1.020
Si*	3.920	0.600	0.785

Note: Si refers to silicon atoms in the SiO_2 substrate, and Si* refers to silicon atoms in OTS molecules.

Bond parameters are provided in Table 3, with the potential function given by Eq. (3):

$$E_{bond} = K_{bond}\left(r - r_0\right)^2 \tag{3}$$

where r_0 is the equilibrium bond distance, and no distinction is made between silicon atoms in the SiO_2 substrate and OTS molecules.

Table 3 Bond parameters

Bond type	K (kcal/mol/Å^2)	r_0 (Å)
C-C	268.000	1.529
C-H	340.000	1.090
C-Si*	119.505	1.840
Si-O	387.170	1.630
O-H	637.606	0.950

Angle parameters are listed in Table 4, with the potential function given by Eq. (4):

$$E_{angle} = K\left(\theta - \theta_0\right)^2 \tag{4}$$

where θ_0 is the equilibrium bond angle, and no distinction is made between silicon atoms in the SiO_2 substrate and OTS molecules.

Table 4 Angle parameters

Angle Type	K (kcal/mol/rad^2)	θ_0 (°)
C-C-C	58.350	112.70
C-C-H	37.500	110.70
H-C-H	33.000	107.80
C-C-Si	57.636	109.45
C-Si-O	56.133	109.47
Si-O-Si	25.048	144.00
Si-O-H	27.347	119.52
O-Si-O	56.133	109.47

Dihedral parameters used in this study are provided in Table 5, with the potential function given by Eq. (5):

$$E_{dihedral} = \frac{1}{2}K_1\left[1+\cos\varphi\right] + \frac{1}{2}K_2\left[1+\cos\left(2\varphi\right)\right] + \frac{1}{2}K_3\left[1+\cos\left(3\varphi\right)\right] + \frac{1}{2}K_4\left[1+\cos\left(4\varphi\right)\right] \tag{5}$$

All other dihedral parameters, including those involving Si atoms, are set to zero.

Table 5 Dihedral parameters

Dihedral Type	K_1 (kcal/mol)	K_2 (kcal/mol)	K_3 (kcal/mol)	K_4 (kcal/mol)
C-C-C-C	1.30	-0.05	0.20	0.00
C-C-C-H	0.00	0.00	0.30	0.00
H-C-C-H	0.00	0.00	0.30	0.00

Simulation details

Simulations were performed using the LAMMPS (Large-scale Atomic/Molecular Massively Parallel Simulator) software[36]. A hydroxylated SiO_2 substrate with initial dimensions of 4.03 × 4.14 nm and a thickness of 5.36 nm was used as the base. Varying numbers of OTS molecules were grafted onto the substrate surface, followed by a 3×3 array expansion in the x and y directions, resulting in a substrate of 12.1 × 12.4 nm with a thickness of 5.4 nm for simulation purposes. Periodic boundary conditions were applied in the x, y, and z directions. The system underwent energy minimization using the conjugate gradient method, followed by a 1 ns relaxation at 300 K in the microcanonical (NVE) ensemble with a time step of 1 fs, controlled by the Berendsen thermostat[37]. In the molecular dynamics simulations of this study, to ensure the reasonableness and effectiveness of the NVE ensemble, the initial structure of the system underwent comprehensive preparation prior to simulation. OTS molecules in the initial configuration were subjected to energy minimization to avoid unreasonable atomic overlaps or extreme conformations, thereby obtaining a stable starting structure. The setup of the initial structure fully considered reasonable molecular spacings and orientations, in line with physical and chemical expectations. Furthermore, after simulation commencement, the selected relaxation time was sufficiently long to allow

the system to reach a state of local thermal equilibrium, thereby ensuring the reliability of subsequent data. This stage facilitated the grafting of OTS molecules onto the SiO_2 substrate surface. The primary objective of this phase was to establish the OTS SAM assembly, rather than to investigate the self-assembly process itself, which would require longer simulation times and additional mechanistic considerations. Long-range Coulomb interactions calculated using the Particle-Particle Particle-Mesh (PPPM) method, with a cutoff radius of 1nm for both interatomic forces and Coulomb interactions. The simulation time step was 1 fs, with a total simulation duration of 4 ns, comprising 3 ns for system equilibration and 1 ns for data collection and density distribution analysis. The canonical (NVT) ensemble was employed, with the system temperature maintained at 300K using the Nosé-Hoover thermostat.

Contact angle determination

The contact angle was calculated using the isodensity curve fitting method. The system was divided into 1 Å × 1 Å × 1 Å cubic grids, and the number of water molecules in each grid was counted to generate a two-dimensional density distribution map. A set of isodensity points near the vapor-liquid interface was selected and fitted to obtain the vapor-liquid interface contour, as illustrated in Fig. 2. The spherical cap height (h), sphere radius (r), and contact circle radius (r^*) were used to compute the contact angle via Eqs (6) and (7):

$$\theta = \arccos\left(\frac{r-h}{r}\right), (h < r) \tag{6}$$

$$\theta = 90° + \arcsin\left(\frac{r-h}{r}\right), (h > r) \tag{7}$$

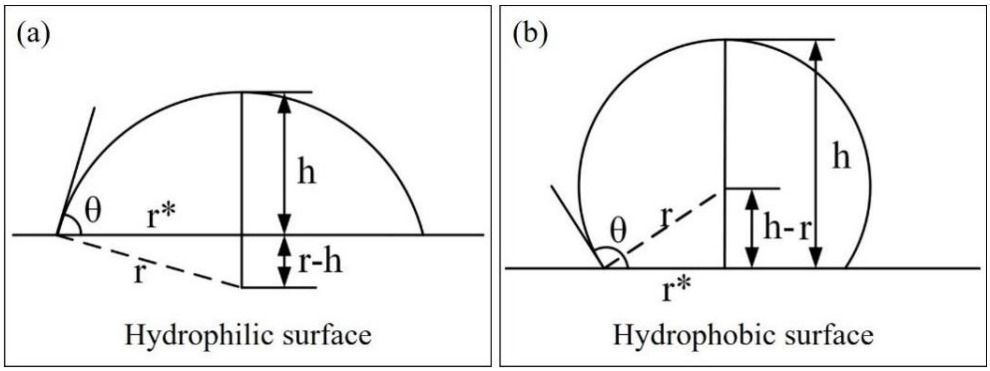

Fig. 2. Schematic of contact angle calculation using isodensity curve fitting: (a) Contact angle on a hydrophilic surface; (b) Contact angle on a hydrophobic surface.

Materials and experiments

The experimental system comprises three primary modules: low-temperature module, operation module, and image acquisition module, as illustrated in Fig. 3. The low-temperature module consists of a semiconductor cooling platform, a low-temperature coolant circulation system, and a temperature sensing system. An acrylic experimental chamber is mounted above the cooling platform to secure samples and minimize environmental interference. A slot in the chamber's top allows the needle of an electric syringe to deliver precise water droplet volumes. The operation module includes the electric syringe, the cooling platform, and the coolant circulation control system. The image acquisition module comprises a camera, a contact angle measurement instrument, and a computer, capturing the icing process of water droplets in a cold environment through the transparent acrylic side panel.

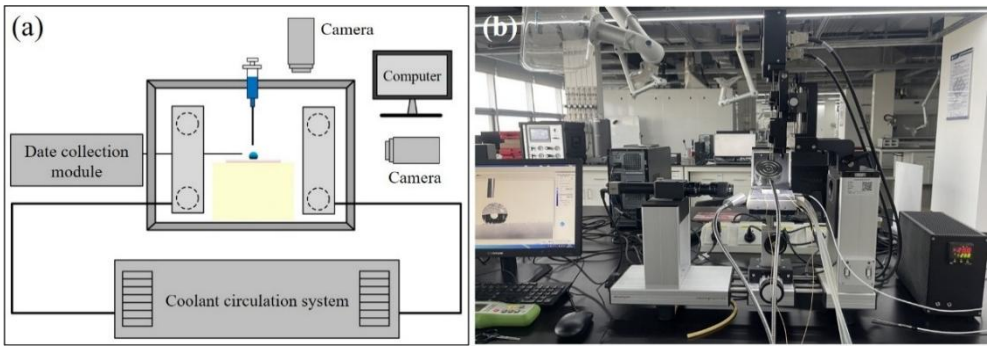

Fig. 3. (a)Schematic diagram and (b) photograph of the Experimental System.

Samples were prepared using 40 × 40 × 5 mm^3 slices of wind turbine blade composite material as substrates. Three surface types were created: hydrophilic SiO_2 coating, hydrophobic OTS coating, and uncoated control, as shown in Fig. 4. Prior to coating, substrates were cleaned to ensure a pristine surface, as depicted in Fig. 4b. The SiO_2 coating was applied via dip-coating, immersing substrates in an ethanol-diluted SiO_2 particle solution for 30 s, followed by drying at 200°C for 20 min, yielding a transparent coating (Fig. 4a). Atomic force microscopy (AFM) analysis of the SiO_2-coated surface revealed a root-mean-square (RMS) roughness of 88.3 nm, indicating subtle surface texturing that supports hydrophilicity. The uncoated substrate exhibited a baseline RMS roughness of 103.3 nm (Fig. 4e), serving as the reference for comparative assessments. The OTS coating was prepared by spray-coating. OTS was mixed with deionized water (1:2 molar ratio), stirred for 3 min, and left to stand for 2 h to complete hydrolysis. After releasing HCl in a ventilated environment, hexane (5% volume) was added, and the mixture was stirred for 2 h. Pre-treated substrates were sprayed uniformly, with the nozzle at an optimal distance to ensure even coverage, and cured at 50°C for 20 min, resulting in a white, high-roughness coating (Fig. 4c). AFM imaging confirmed successful OTS grafting, with an increased RMS roughness of

163.8 nm (Fig. 4f), attributable to the self-assembled monolayer's ordered alkyl chain structure and potential micro-roughness from spray deposition. These roughness values, derived from 20 × 20 μm² scan areas, provide quantitative evidence of the distinct surface morphologies across the samples, correlating with their wetting behaviors.

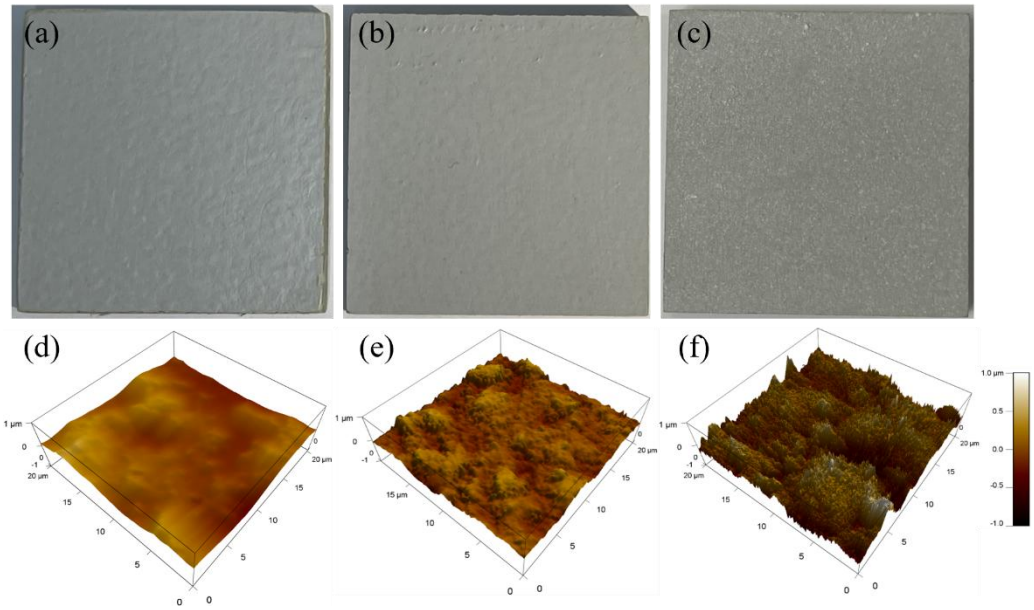

Fig. 4. Photographs and AFM images of prepared samples: (a, d) SiO_2 hydrophilic coating; (b, e) Uncoated substrate; (c, f) OTS hydrophobic coating.

Static water contact angles were measured using the OCA-20 instrument, as shown in Fig. 5a-c. For each surface, six random locations were tested with 4 μL deionized water droplets, and average contact angles were calculated. The SiO_2-coated surface exhibited a contact angle of 17.1 ± 0.5°, indicating strong hydrophilicity. The uncoated surface showed 82.3 ± 1.8°, suggesting near-neutral wetting. The OTS-coated surface displayed 151.2 ± 1.5°, confirming strong hydrophobicity. Contact angles with error bars are presented in Fig. 5d, representing hydrophilic, neutral, and hydrophobic wetting behaviors for subsequent icing experiments.

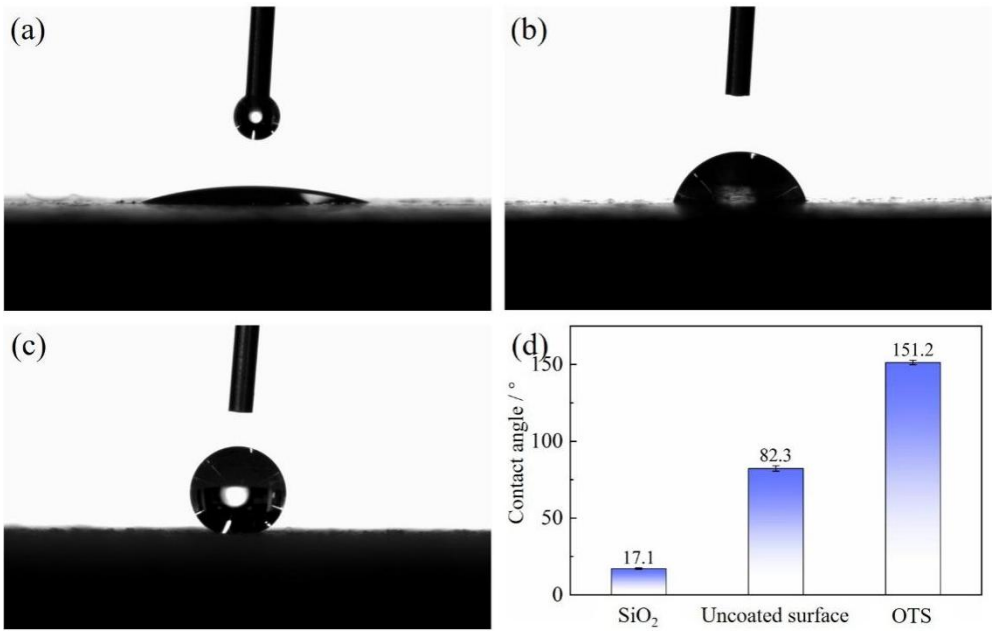

Fig. 5. Contact angle measurement process: (a) SiO_2 hydrophilic coating; (b) Uncoated substrate; (c) OTS hydrophobic coating. (d) Static water contact angles of the three sample types.

Result and discussion

Effect of OTS coverage density on monolayer thickness

Fig. 6. illustrates the simulated OTS monolayer structures at low, medium, and high coverage densities. The thickness of the OTS monolayer varies with coverage density. Monolayer thickness is defined as the average distance between the oxygen atoms of the substrate bonded to alkylsilane molecules and the terminal atoms of the hydrocarbon tail, projected along the direction perpendicular to the surface. The theoretical maximum thickness of OTS SAMs on SiO_2, calculated from standard bond lengths, covalent radii, and van der Waals radii, is 2.62 nm[13, 28]. However, experimental measurements report a value closer to 2.4 nm[38], which is adopted in this study as the extended molecular length of OTS. To calculate the average monolayer thickness, the

xy plane was divided into 20 Å × 20 Å grid cells. For each cell, the highest z-coordinate of carbon atoms in OTS molecules and the z-coordinate of Si atoms were averaged, and their difference was taken as the monolayer thickness. At a tilt angle of 0°, the coating thickness is assumed to equal the molecular length of 2.4 nm. The average molecular tilt angle was determined by calculating the cosine of the angle between the average monolayer thickness and the molecular length.

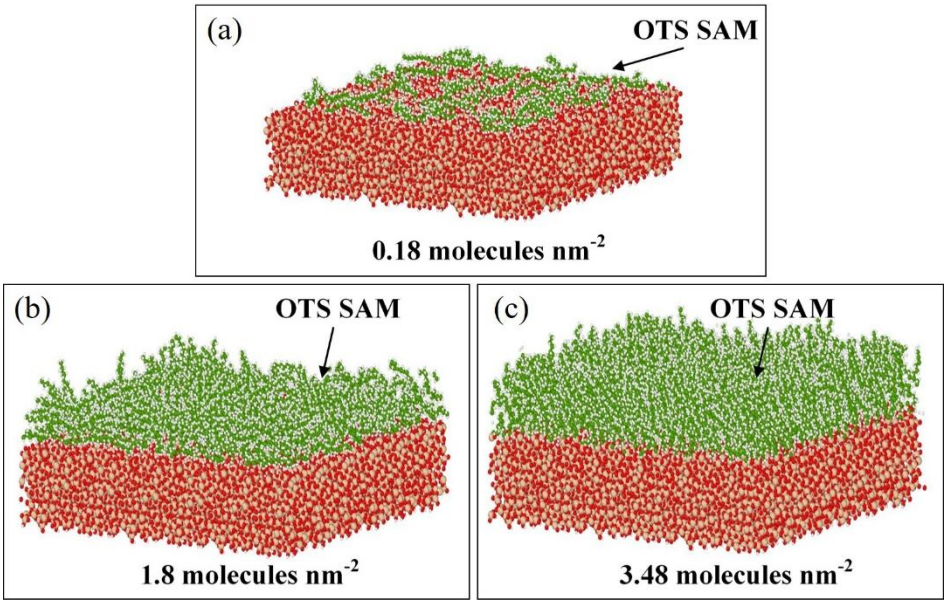

Fig. 6. OTS monolayer structures at different coverage densities: (a) Low coverage density; (b) Medium coverage density; (c) High coverage density.

Statistical analysis of monolayer thickness and average molecular tilt angle across all coverage densities is presented in Fig. 7. At low coverage densities (e.g., 0.18 molecules nm^{-2}), the average monolayer thickness is approximately 0.3 nm, with tilt angles ranging from 75° to 85°. This is attributed to the strong dependence of OTS long-chain molecules on the SiO_2 substrate, causing molecules to lie nearly flat on the surface. As coverage density increases from 0.90 to 2.51 molecules nm^{-2}, the tilt angle decreases to approximately 40°, reflecting limited surface attachment space. The

increased molecular density forces OTS chains to rely on intermolecular interactions, preventing complete collapse onto the substrate. Beyond 2.51 molecules nm^{-2}, intermolecular reliance becomes more pronounced, with tilt angles decreasing to ~20° at 3.48 molecules nm^{-2}, approaching near-perpendicular configurations. This trend aligns with previous studies on alkylsilane chains of varying lengths [31, 39], validating the reliability of the OTS monolayer grafting simulations.

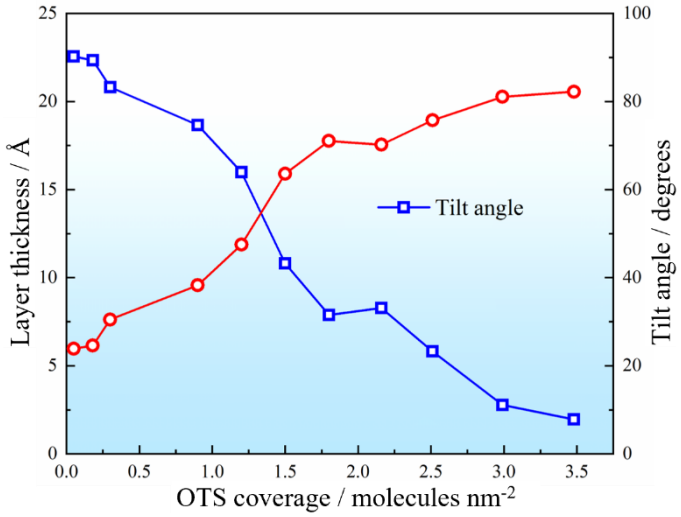

Fig. 7. Average monolayer thickness and molecular tilt angle.

Effect of water molecule number on contact angle

The number of water molecules in molecular dynamics simulations significantly influences the accuracy of wetting behavior predictions. To investigate this effect, the relationship between water molecule count and contact angle was examined using nanoscale droplets modeled by filling a face-centered cubic (FCC) lattice with water molecules. Droplet size was varied to achieve water molecule counts ranging from 429 to 7,060, with simulations conducted on a substrate grafted with an OTS SAM at a coverage density of 3.48 molecules nm^{-2}. Simulations were performed in the canonical (NVT) ensemble at 300 K, controlled by the Nosé-Hoover thermostat, with a total

duration of 4 ns to reach steady-state conditions. The resulting oxygen atom mass density distributions for the nanoscale droplets are presented in Fig. 8.

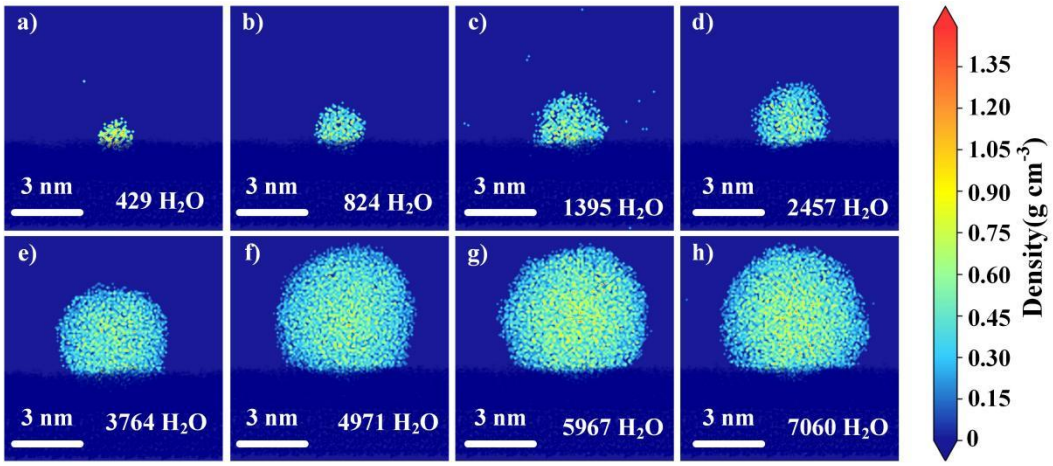

Fig. 8. Oxygen atom mass density distribution of nanoscale droplets on SAM surfaces under different numbers of water molecules: (a) 429, (b) 824, (c) 1395, (d) 2457, (e) 3764, (f) 4971, (g) 5967, (h) 7060. The color bar represents the mass density of oxygen atoms in water molecules (g cm^{-3}).

Contact angles were calculated using the isodensity curve fitting method, and the relationship between water molecule number and contact angle is shown in Fig. 9. At water molecule counts below 3,300, simulated contact angles are consistently smaller than expected, occasionally exhibiting hydrophilic behavior (contact angles < 90°). These angles also show significant variability with changes in molecule count. This deviation is attributed to enhanced molecular motion at 300 K, which destabilizes the droplet shape at low molecule counts, preventing accurate representation of the hydrophobic nature of the OTS SAM. For water molecule counts between 3,300 and 7,060, contact angles stabilize around 132.5°, exhibiting high consistency and minimal variation with molecule count. This value closely aligns with experimental

measurements of OTS SAMs[40], confirming that simulations with more than 3,300 water molecules reliably capture the hydrophobic properties of the OTS monolayer. To optimize computational efficiency while maintaining accuracy, a droplet size of 3,764 water molecules was selected for subsequent simulations, balancing the trade-off between system size and relaxation time requirements.

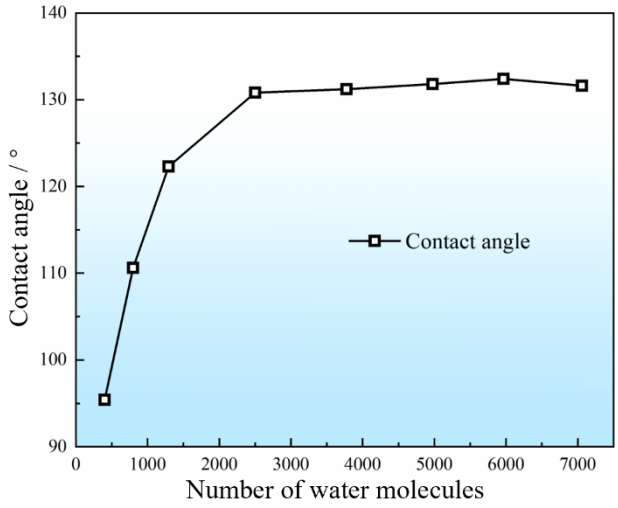

Fig. 9. Relationship between water molecule number and contact angle.

Effect of OTS coverage density on droplet contact angle and rolling friction

Nanoscale droplets were assembled with substrates at various OTS coverage densities, maintaining a droplet center-of-mass distance of 3.4 nm from the substrate surface. Simulations used periodic boundary conditions in the x, y, and z directions, conducted in the NVT ensemble at 300 K with a 1 fs time step, relaxing for 4 ns to reach a steady state. Fig. 10a shows the steady-state wetting result at an OTS coverage density of 0.9 molecules nm^{-2}. Water molecule mass density was calculated using a density distribution method. A circular arc was fitted to the droplet density distribution edge, with the baseline set at the average SAM height, to determine the static contact angle, as shown in Fig. 10b.

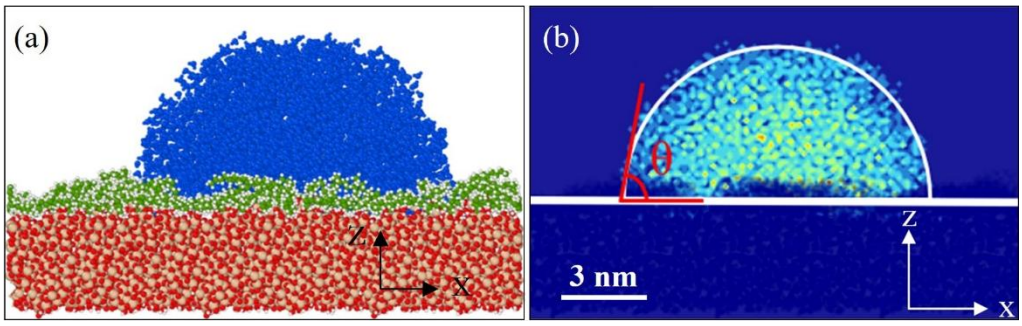

Fig. 10. Wetting simulation results at OTS coverage density of 0.9 molecules nm^{-2}: (a) Simulation snapshot; (b) Contact angle fitting process.

Wetting states across different coverage densities are summarized in Fig. 11a-j, with droplet mass density distributions peaking around 0.8 g cm^{-3}. As OTS coverage density increases, the contact angle of nanoscale droplets rises, transitioning the substrate from superhydrophilic to hydrophobic between 0.9 and 1.5 molecules nm^{-2}. Notably, at a coverage density of 1.80 molecules nm^{-2}, the contact angle reaches 125.2°, surpassing values observed at 2.16 and 2.51 molecules nm^{-2}, deviating from the overall trend. To investigate this anomaly, surface roughness, defined as the standard deviation of monolayer thickness[41], was calculated for different coverage densities. Surface wettability is governed by both the chemical composition and microscopic geometry of the solid surface[42, 43]. Fig. 11k and l show the roughness details at coverage densities of 1.8 molecules nm^{-2} and 2.51 molecules nm^{-2}.

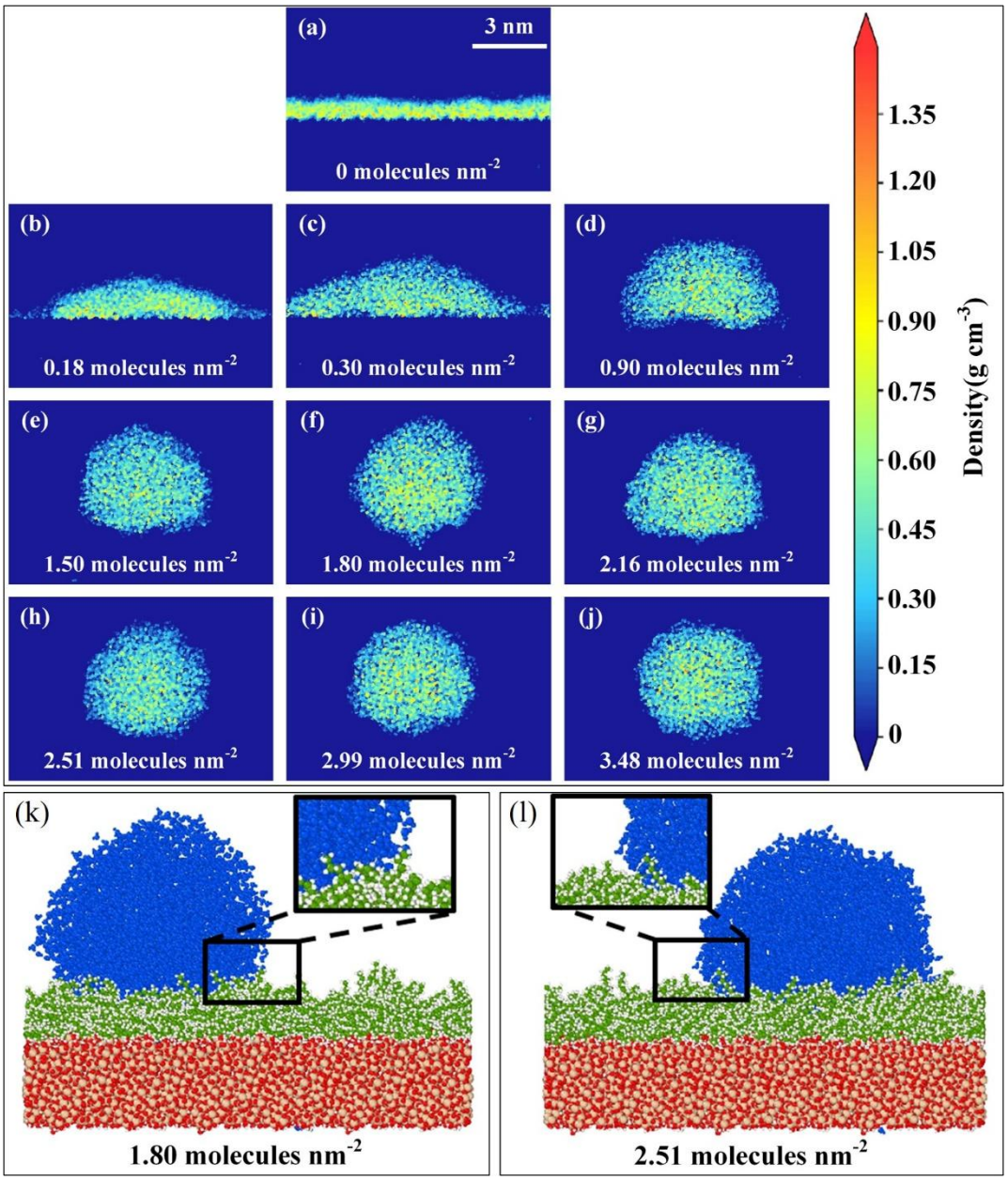

Fig. 11. Oxygen atom mass density distribution of nanoscale droplets: (a) Wetting behavior on a bare SiO_2 substrate (control); (b)-(j) Wetting states at OTS coverage densities from 0.18 to 3.48 molecules nm^{-2}, with the color bar representing the mass density of oxygen atoms in water molecules (g cm^{-3}). (k), (l) Surface roughness.

Contact angle and surface roughness data, derived from isodensity curve fitting, are plotted as a function of OTS coverage density in Fig. 12. The contact angle increases with increasing OTS coverage density, from 0° on a bare SiO_2 substrate (0 molecules

nm^{-2}) to 132.7° at 3.48 molecules nm^{-2}, closely matching the experimentally reported value of 132.92°[40]. Beyond 2.51 molecules nm^{-2}, further increases in coverage density yield diminishing returns, with the contact angle approaching a plateau near 133°, indicating saturation of the hydrophobic effect in high-density OTS SAMs. In contrast, surface roughness, defined as the standard deviation of monolayer thickness[41], exhibits a non-monotonic trend. Roughness peaks at 0.262 nm at a coverage density of 1.80 molecules nm^{-2} and decreases to 0.122 nm at 3.48 molecules nm^{-2}. This synergy results in a microstructure that elevates the droplet, enhancing hydrophobicity and yielding a larger contact angle. This behavior is consistent with a transition from the Wenzel model[44] to the Cassie-Baxter model[45], where peak roughness amplifies hydrophobicity via reduced contact area, consistent with increasing monolayer thickness and evolving tilt angles (Fig. 7 and Fig. 12). Beyond 1.80 molecules nm^{-2}, surface roughness decreases, yet hydrophobicity continues to increase, indicating that the intrinsic properties of OTS molecules, rather than microstructural effects, dominate the hydrophobic performance at higher coverage densities.

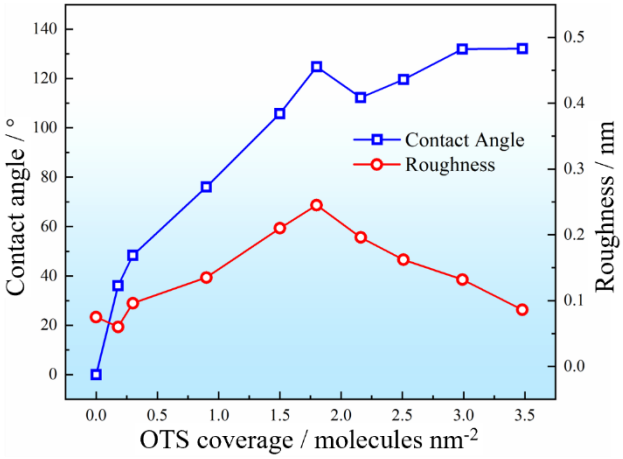

Fig. 12. Simulated droplet contact angle and surface roughness.

The spreading behavior of nanoscale droplets at low OTS coverage density reveals a notable interaction with the substrate. Fig. 13 presents a top-down view of the wetting process at 0.18 molecules nm^{-2}, with the SiO_2 substrate rendered in brown, OTS carbon atoms in green, hydrogen atoms in white, and water molecules in blue. From 0 to 1.4 ns, water molecules form a distinct "vacuum ring" around OTS molecules, indicating hindered spreading due to the combined effects of OTS hydrophobicity and surface morphology.

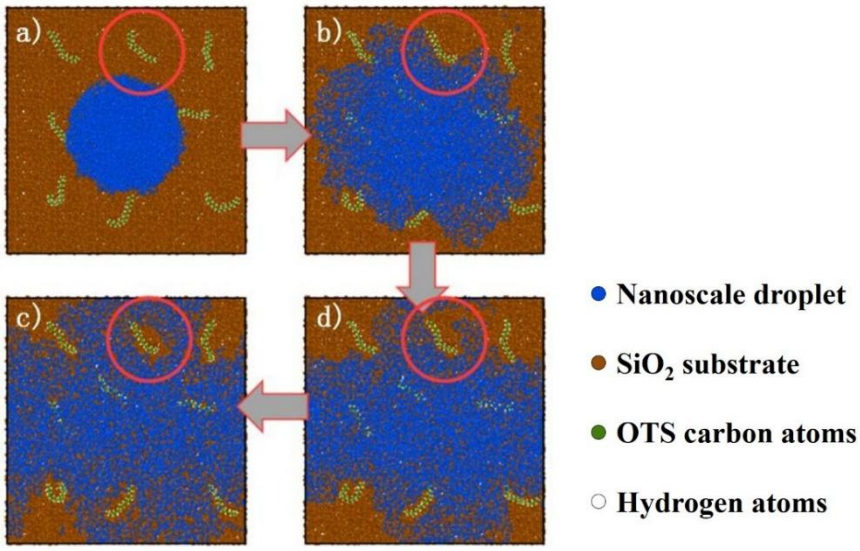

Fig. 13. Top-down view of nanoscale droplet spreading at OTS coverage density of 0.18 molecules nm^{-2}: (a) 0 ns, (b) 0.7 ns, (c) 1.4 ns, (d) 2.8 ns.

To further explore this phenomenon, droplet rolling behavior was simulated on tilted substrates to investigate the interaction dynamics between droplets and OTS molecules. Four representative coverage densities were selected: 0.18, 0.90, 1.50, and 3.48 molecules nm^{-2}, corresponding to extremely low, low, medium, and high coverage, respectively. After system equilibration, a constant force of 0.001 kcal/mol/Å (6.95×10^{-5} μN) was applied along the x-direction to each water molecule's oxygen atom.

Simulations were conducted in the NVT ensemble at 300 K for 1 ns with a 1 fs time step. At 0.18 molecules nm^{-2}, no rolling occurred, while at higher density, the droplet's upper tilt decreased, and rolling speed increased with coverage density, as shown in Fig. 14. The contact line, marked in pink, shortens with increasing coverage density, and the difference between advancing (θ_a) and receding (θ_r) angles diminishes, consistent with reduced contact angle hysteresis on hydrophobic surfaces. Contact angle hysteresis, defined as the difference between advancing and receding angles, reflects surface adhesion strength. Larger hysteresis indicates stronger adhesion, while reduced hysteresis facilitates easier droplet sliding.

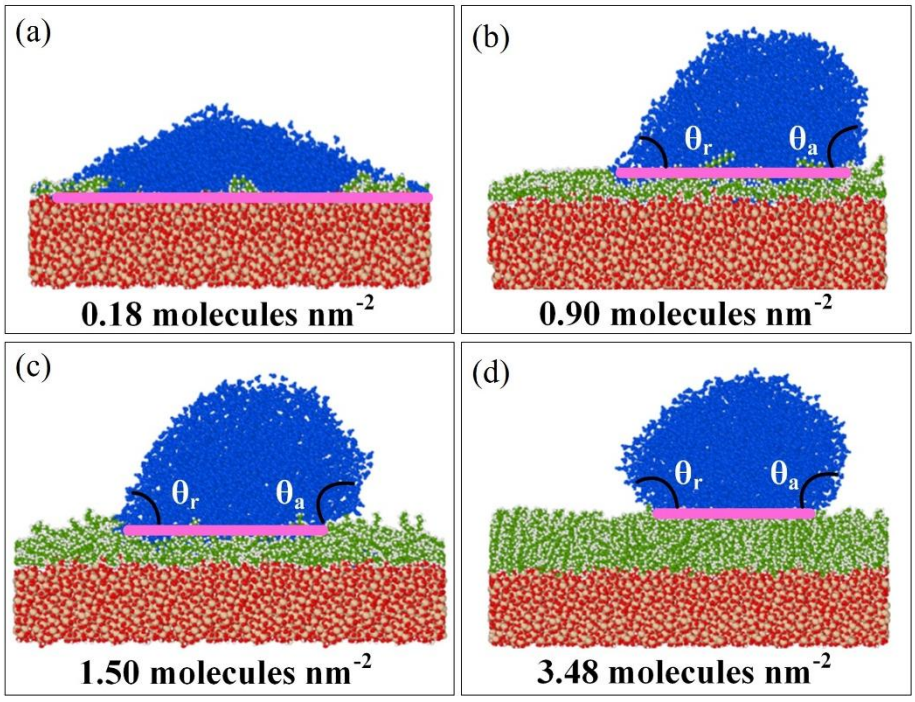

Fig. 14. Transient snapshots of droplet rolling: (a)-(d) Rolling behavior at OTS coverage density from 0.18 to 3.48 molecules nm^{-2}, with no rolling observed at 0.18 molecules nm^{-2}. Advancing (θ_a) and receding (θ_r) angles are indicated.

Fig. 15 illustrates trends in average rolling friction and center-of-mass velocity. As coverage density increases, the average velocity over 2 ns rises from 4.894 m/s to

41.291 m/s, reflecting faster droplet motion on more hydrophobic surfaces. Surface friction decreases significantly, driven by the formation of a more uniform and denser OTS monolayer, which reduces the droplet-substrate interaction strength and rolling resistance. At low coverage density, irregularly distributed OTS molecules create high friction, slowing droplet motion. As coverage density increases, the smoother, more hydrophobic surface reduces contact area and friction, accelerating rolling. This behavior is consistent with the transition from the Wenzel state to the Cassie-Baxter state, where decreased roughness and enhanced hydrophobicity lower rolling resistance[42, 46]. These findings elucidate the wetting and frictional properties of OTS SAMs, demonstrating that increased hydrophobicity reduces rolling friction, with implications for designing anti-icing coatings and self-cleaning materials.

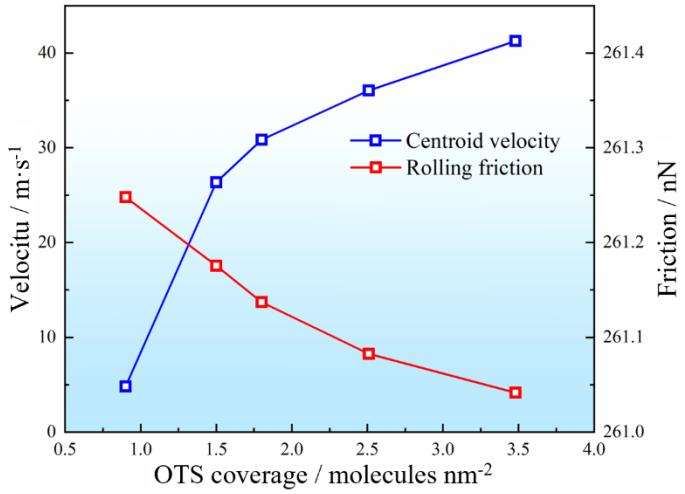

Fig. 15. Average center-of-mass velocity and rolling friction across OTS coverage densities.

Self-driven droplet jumping on OTS monolayers

Droplet jumping has been shown to enhance anti-frost properties by reducing surface droplet density, thereby inhibiting ice bridge formation and delaying frost

propagation[47]. To investigate the low-friction properties of OTS SAMs for self-cleaning applications, simulations of self-driven droplet jumping were conducted to elucidate the microscopic mechanisms underlying their anti-frost capabilities. Simulations were performed at 300 K in the canonical (NVT) ensemble, using the Nosé-Hoover thermostat and the Particle-Particle Particle-Mesh (PPPM) method for long-range interactions. Four water droplets with diameters of 10 Å, 15 Å, 18 Å, and 20 Å (containing ~125, 343, 578, and 785 water molecules, respectively) were initialized with center-of-mass separations of 30 Å in the x/y directions across all three coverage scenarios (0.18, 1.80, and 3.48 molecules nm^{-2}). The simulation used a 1 fs time step and a total duration of 1.2 ns to explore self-driven droplet jumping behavior.

Fig. 16 illustrates the droplet jumping behavior at low (0.18 molecules nm^{-2}), medium (1.80 molecules nm^{-2}), and high (3.48 molecules nm^{-2}) OTS coverage densities. At medium and high coverage densities, droplet jumping is observed, with the four droplets merging under intermolecular forces within 1.2 ns, resulting in fewer droplets by the simulation's end. At 0.18 molecules nm^{-2} (Fig. 16a), droplets spread rapidly on the substrate by 0.12 ns, begin contacting at their boundaries by 0.17 ns, and connect by 0.8 ns. However, due to the hydrophobic effect of OTS molecules, the droplets do not form a cohesive wetting state, instead avoiding OTS molecules. By 1.2 ns, the droplet configuration stabilizes, resembling the 0.8 ns state. At 1.80 molecules nm^{-2} (Fig. 16b), the two largest droplets initiate contact by 0.33 ns, merge by 0.47 ns, and the third-largest droplet begins merging with the larger droplet by 0.96 ns, forming a single large droplet. The smallest droplet remains unmerged, and the system stabilizes

by 1.2 ns. At 3.48 molecules nm^{-2} (Fig. 16c), merging occurs most rapidly, with the two largest droplets contacting by 0.16 ns, completing merger by 0.3 ns, and the third droplet joining by 0.87 ns. By 1.1 ns, the merger is complete, with the smallest droplet showing minimal displacement, and the system stabilizes by 1.2 ns.

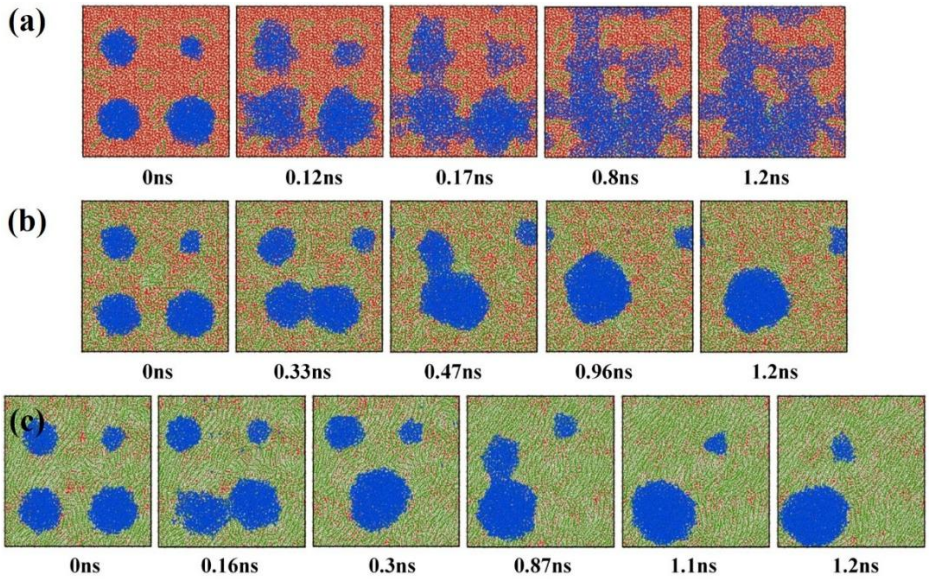

Fig. 16. Simulation of self-driven droplet jumping on OTS monolayers: (a) 0.18 molecules nm^{-2}; (b) 1.80 molecules nm^{-2}; (c) 3.48 molecules nm^{-2}.

Droplet behavior is strongly influenced by OTS coverage density. At medium and high coverage densities, the hydrophobic OTS surface reduces droplet-substrate interactions, promoting droplet coalescence driven by intermolecular forces such as surface tension and van der Waals interactions. This results in faster merging times at higher coverage density, where stronger intermolecular forces accelerate droplet convergence. At 3.48 molecules nm^{-2}, the rapid merging reflects enhanced hydrophobicity, while at 1.80 molecules nm^{-2}, merging is slower, indicating the role of intermolecular force strength in droplet dynamics. In contrast, at 0.18 molecules nm^{-2}, the predominantly hydrophilic substrate leads to small contact angles, causing droplets

to spread and connect without forming a cohesive spherical droplet, thus failing to achieve self-cleaning behavior. This aligns with prior studies[47], confirming that low coverage density hinders effective droplet jumping. The hydrophobic nature of OTS SAMs at medium and high coverage densities minimizes droplet spreading and promotes spontaneous coalescence, facilitating self-cleaning. These findings highlight the potential of OTS SAMs for anti-frost and self-cleaning applications by leveraging their ability to induce droplet jumping without external forces.

Experimental validation of icing and de-icing performance

The icing process of water droplets on cold surfaces involves two critical stages. The initial moment of droplet contact with the surface is defined as 0 s, with the droplet initially spherical. As it spreads and wets the cold surface, its temperature decreases below the freezing point (0°C). At a specific moment, ice nucleation occurs, followed by rapid dendrite growth, transitioning the droplet from a fully liquid state to an ice-water mixture, a phenomenon known as nucleation-recalescence. The time difference between the initial contact and nucleation-recalescence is defined as the icing delay time. Subsequently, ice ridges grow from the droplet's base to its top, forming a fully frozen droplet with a peach-shaped tip due to ice's lower density and reduced surface tension at the top. The time difference between initial contact and complete freezing is defined as the complete icing time. Icing delay time and complete icing time are key metrics for evaluating anti-icing performance. To assess these, samples with SiO_2 hydrophilic coating, OTS hydrophobic coating, and an uncoated control were fixed on the cooling platform of the experimental system. Temperature sensors monitored the

surface temperature, stabilized at -10°C. 4 μL deionized water droplet was deposited on each surface, and the icing process was recorded using a digital camera to measure icing delay time and complete icing time.

Fig. 17 illustrates the icing process on the three surfaces. On the SiO_2 hydrophilic coating, the droplet spreads rapidly and nucleates within a short time, transitioning from transparent to opaque by 12 s, with ice ridges growing upward (indicated by red dashed lines) and forming a peach-shaped tip by 17 s, indicating complete icing. On the uncoated surface, nucleation occurs at 92 s, with ice ridges growing upward and complete icing achieved by 121 s. On the OTS hydrophobic coating, the icing delay is significantly longer, with nucleation observed at the lower-right corner at 649 s, followed by a 76 s ice ridge growth period, reaching complete icing at 725 s.

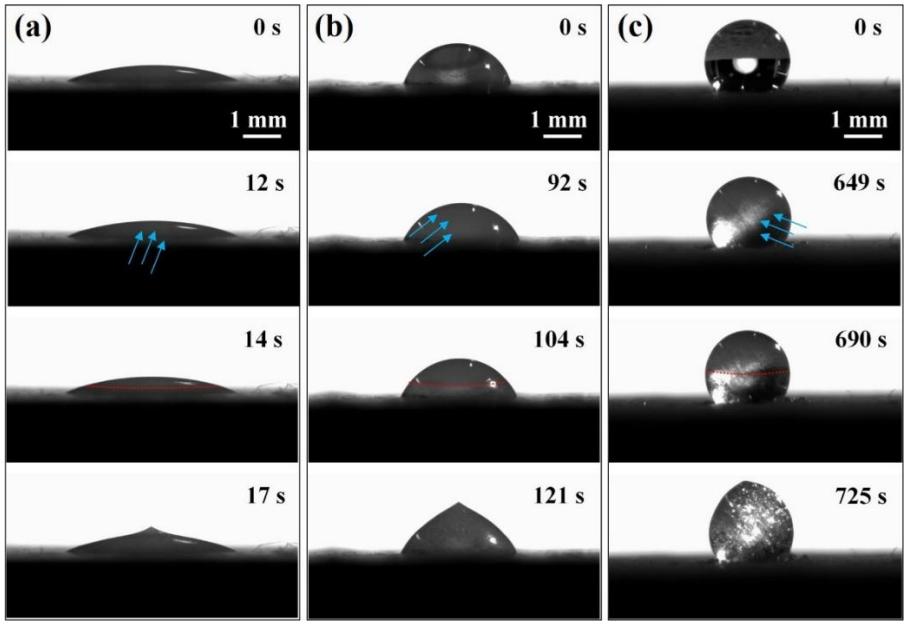

Fig. 17. Icing process of water droplets on different surfaces: (a) SiO_2 hydrophilic coating; (b) Uncoated substrate; (c) OTS hydrophobic coating.

Fig. 18 presents the average icing delay and complete icing times from three experiments per surface, with error bars below 30 s, indicating high surface stability

and result reliability. Surfaces with larger contact angles (i.e., greater hydrophobicity) exhibit significantly longer icing delay and complete icing times. The OTS hydrophobic coating outperforms the SiO_2 hydrophilic and uncoated surfaces, consistent with simulation. The prolonged icing delay on hydrophobic surfaces arises from two primary factors: (1) larger contact angles reduce the droplet-surface contact area, lowering the heat transfer rate, as corroborated by simulations; (2) the higher roughness of the OTS coating traps air within surface microstructures, further reducing heat transfer compared to the smoother SiO_2 and uncoated surfaces. Additionally, classical nucleation theory suggests that the low surface energy of OTS increases the energy barrier for ice nucleation, contributing to the extended icing delay. These combined effects confirm the superior anti-icing performance of the OTS coating.

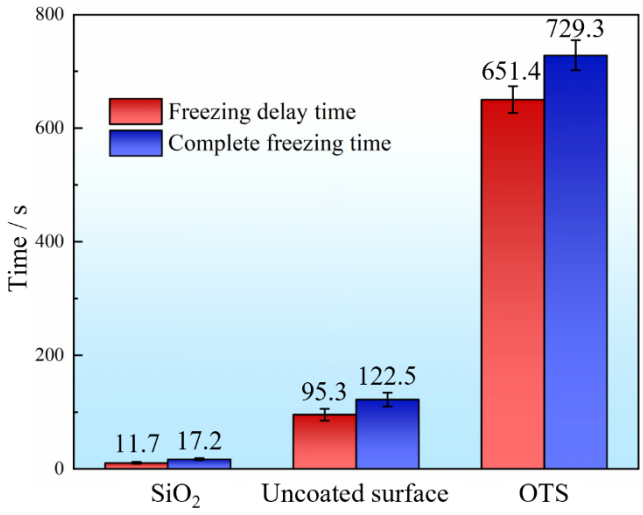

Fig. 18. Icing delay and complete icing times on different surfaces.

While the OTS hydrophobic coating excels in delaying icing, practical applications under complex conditions require effective de-icing capabilities. De-icing experiments were conducted by raising the cooling platform temperature from -10°C to 10°C after complete droplet freezing, recording the melting process of ice droplets on

each surface. Fig. 19 shows the melting process on the different surfaces. On the SiO_2 hydrophilic coating, ice droplets melt rapidly within 13 s but remain stationary, re-freezing upon recooling. On the uncoated surface, complete melting occurs at 98 s, attributed to a reduced contact area slowing heat transfer. On the OTS hydrophobic coating, melting takes 215 s, 2.19 times longer than the uncoated surface and significantly longer than the hydrophilic surface. Melting times are generally shorter than icing times due to the lower energy required to heat from -10°C to above 0°C compared to cooling from 22°C to below 0°C. The reversible nature of phase transitions results in similar heat transfer rates for icing and melting, with contact area and surface roughness influencing both processes. The OTS coating's minimal contact area and high roughness, with air trapped in microstructures, further reduce heat transfer rates, leading to the longest melting time.

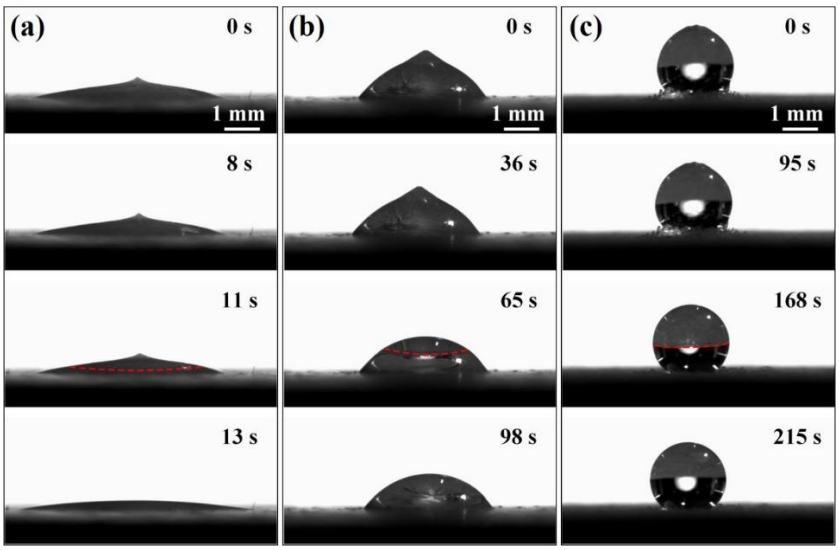

Fig. 19. Melting process of ice droplets on different surfaces: (a) SiO_2 hydrophilic coating; (b) Uncoated substrate; (c) OTS hydrophobic coating.

Although hydrophobic surfaces exhibit slower melting, practical conditions for high-altitude equipment often involve non-horizontal or dynamic surfaces. To simulate

these, de-icing experiments on a 15° tilted surface were conducted without active heating, allowing the system to warm naturally to room temperature after stopping refrigeration, with 0 s defined as the moment refrigeration ceased. Fig. 20 depicts the melting and removal process on tilted surfaces. On the SiO_2 hydrophilic surface, ice droplets fully melt by 42 s but remain stationary. On the uncoated surface, melting completes by 124 s, with minimal droplet displacement and no detachment. On the OTS hydrophobic surface, melting begins at the base by 50 s, forming a thin water layer that lubricates the interface between the unmelted ice and the surface. By 56 s, the ice droplet rotates and slides, achieving significant displacement within 2 s and detaching by 58 s, only 1.38 times the hydrophilic surface's melting time. This rapid detachment leverages the low rolling friction of OTS surfaces (Section 3.3), where the water layer facilitates sliding under gravitational or external forces, enabling ice removal without complete melting.

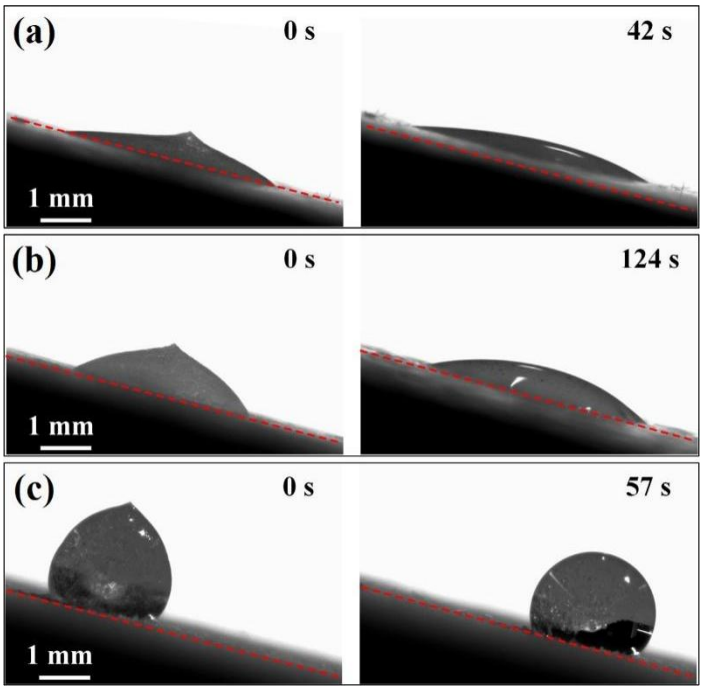

Fig. 20. Melting and removal process of ice droplets on tilted surfaces: (a) SiO_2

hydrophilic coating; (b) Uncoated substrate; (c) OTS hydrophobic coating.

Comparing horizontal and tilted surface experiments, hydrophilic surfaces exhibit the fastest melting on horizontal surfaces, followed by uncoated and OTS hydrophobic surfaces, due to differences in contact area and roughness affecting heat transfer. However, on tilted surfaces simulating real-world conditions, the OTS coating enables ice detachment in significantly less time than full melting, validating its superior de-icing performance. This is attributed to the formation of a lubricating water layer and low-friction properties, making OTS coatings highly effective for anti-icing and de-icing applications in dynamic environments.

Conclusion

Molecular dynamics simulations were employed to investigate the performance of OTS SAM coatings grafted onto SiO_2 substrates, focusing on key parameters such as monolayer thickness, average molecular tilt angle, wettability, and droplet rolling friction. Additionally, an experimental system based on a semiconductor cooling platform was designed and constructed to evaluate the icing characteristics and ice removal capabilities of surfaces with varying wettability. The primary findings are summarized as follows:

(1) OTS SAM thickness increases with coverage density, from 0.3 nm at 0.18 molecules nm^{-2} to approximately 2.4 nm at 3.48 molecules nm^{-2}. Molecular tilt angles decrease from 75–85° at low coverage to 40° at medium coverage, then increase to 85° at high coverage due to steric effects.

(2) Contact angles of nanoscale droplets rise with OTS coverage density, from 0° on bare SiO_2 to 132.7° at 3.48 molecules nm^{-2}. A notable increase to 125.2° at 1.80 molecules nm^{-2} results from combined hydrophobicity and peak surface roughness of 0.262 nm. Simulations with 3,764 water molecules effectively capture hydrophobic behavior.

(3) At low coverage, droplet spreading forms a "vacuum ring" around OTS molecules. Rolling friction decreases as coverage density increases, with droplet velocity rising from 4.894 m/s to 41.291 m/s. Self-driven droplet jumping at medium and high coverage densities enables rapid coalescence, supporting self-cleaning functionality.

(4) Experiments on wind turbine blade composite samples show that OTS coatings extend icing delay time to 649 s and complete icing time to 725 s, compared to 12 s and 17 s for SiO_2 hydrophilic coatings, and 92 s and 121 s for uncoated surfaces. This is due to reduced contact area, high roughness, and low surface energy. In de-icing tests, OTS coatings require 215 s for complete melting on horizontal surfaces but achieve ice detachment in 58 s on a 15° tilted surface via a lubricating water layer, leveraging low friction for efficient ice removal.

Acknowledgements

This work was financially supported by the National Science and Technology Major Project (Grant No. J2020-V-0004-0030).

Reference

(1) Bigelow, W. C.; Pickett, D. L.; Zisman, W. A. Oleophobic monolayers: I. Films adsorbed from solution in non-polar liquids. *J. Colloid Sci.* **1946**, *1* (6), 513-538. DOI: https://doi.org/10.1016/0095-8522(46)90059-1.

(2) Lessel, M.; Bäumchen, O.; Klos, M.; Hähl, H.; Fetzer, R.; Paulus, M.; Seemann, R.; Jacobs, K. Self‐assembled silane monolayers: an efficient step‐by‐step recipe for high‐quality, low energy surfaces. *Surf. Interface Anal.* **2015**, *47* (5), 557-564. DOI: https://doi.org/10.1002/sia.5729.

(3) Eisert, F.; Gurka, M.; Legant, A.; Buck, M.; Grunze, M. Detection of Molecular Alignment in Confined Films. *Science* **2000**, *287* (5452), 468-470. DOI: https://doi.org/10.1126/science.287.5452.468.

(4) Cione, A. M.; Mazyar, O. A.; Booth, B. D.; McCabe, C.; Jennings, G. K. Deposition and Wettability of [bmim][triflate] on Self-Assembled Monolayers. *J. Phys. Chem. C* **2009**, *113* (6), 2384-2392. DOI: https://doi.org/10.1021/jp808098w.

(5) Britt, D. W.; Hlady, V. An AFM Study of the Effects of Silanization Temperature, Hydration, and Annealing on the Nucleation and Aggregation of Condensed OTS Domains on Mica. *Journal of Colloid and Interface Science* **1996**, *178* (2), 775-784. DOI: https://doi.org/10.1006/jcis.1996.0177.

(6) Chaudhury, M. K.; Whitesides, G. M. Correlation Between Surface Free Energy and Surface Constitution. *Science* **1992**, *255* (5049), 1230-1232. DOI: https://doi.org/10.1126/science.255.5049.1230.

(7) Ding, J. N.; Wong, P. L.; Yang, J. C. Friction and fracture properties of polysilicon coated with self-assembled monolayers. *Wear* **2006**, *260* (1), 209-214. DOI: https://doi.org/10.1016/j.wear.2005.02.060.

(8) Helmy, R.; Fadeev, A. Y. Self-Assembled Monolayers Supported on TiO2: Comparison of C18H37SiX3 (X = H, Cl, OCH3), C18H37Si(CH3)2Cl, and C18H37PO(OH)2. *Langmuir* **2002**, *18* (23), 8924-8928. DOI: https://doi.org/10.1021/la0262506.

(9) Zhang, X.; Liu, X.; Wu, X.; Min, J. Impacting-freezing dynamics of a supercooled water droplet on a cold surface: Rebound and adhesion. *Int. J. Heat Mass Transfer* **2020**, *158*, 119997. DOI: https://doi.org/10.1016/j.ijheatmasstransfer.2020.119997.

(10) Wilson, K. A.; Finch, C. A.; Anderson, P.; Vollmer, F.; Hickman, J. J. Whispering gallery mode biosensor quantification of fibronectin adsorption kinetics onto alkylsilane monolayers and interpretation of resultant cellular response. *Biomaterials* **2012**, *33* (1), 225-236. DOI: https://doi.org/10.1016/j.biomaterials.2011.09.036.

(11) Bäumchen, O.; Fetzer, R.; Klos, M.; Lessel, M.; Marquant, L.; Hähl, H.; Jacobs, K. Slippage and nanorheology of thin liquid polymer films. *J. Phys.: Condens. Matter* **2012**, *24* (32), 325102. DOI: https://doi.org/10.1088/0953-8984/24/32/325102.

(12) Färm, E.; Kemell, M.; Ritala, M.; Leskelä, M. Selective-area atomic layer deposition with microcontact printed self-assembled octadecyltrichlorosilane monolayers as mask layers. *Thin Solid Films* **2008**, *517* (2), 972-975. DOI: https://doi.org/10.1016/j.tsf.2008.08.191.

(13) Wasserman, S. R.; Tao, Y. T.; Whitesides, G. M. Structure and reactivity of

alkylsiloxane monolayers formed by reaction of alkyltrichlorosilanes on silicon substrates. *Langmuir* **1989**, *5* (4), 1074-1087. DOI: https://doi.org/10.1021/la00088a035.
(14) Iwasa, J.; Kumazawa, K.; Aoyama, K.; Suzuki, H.; Norimoto, S.; Shimoaka, T.; Hasegawa, T. In Situ Observation of a Self-Assembled Monolayer Formation of Octadecyltrimethoxysilane on a Silicon Oxide Surface Using a High-Speed Atomic Force Microscope. *J. Phys. Chem. C* **2016**, *120* (5), 2807-2813. DOI: https://doi.org/10.1021/acs.jpcc.5b11460.
(15) Ma, H.; Acton, O.; Hutchins, D. O.; Cernetic, N.; Jen, A. K. Multifunctional phosphonic acid self-assembled monolayers on metal oxides as dielectrics, interface modification layers and semiconductors for low-voltage high-performance organic field-effect transistors. *Phys. Chem. Chem. Phys.* **2012**, *14* (41), 14110-14126. DOI: https://doi.org/10.1039/c2cp41557g.
(16) Sagiv, J. Organized monolayers by adsorption. 1. Formation and structure of oleophobic mixed monolayers on solid surfaces. *Journal of the American Chemical Society* **1980**, *102* (1), 92-98. DOI: https://doi.org/10.1021/ja00521a016.
(17) Gutfreund, P.; Bäumchen, O.; Fetzer, R.; van der Grinten, D.; Maccarini, M.; Jacobs, K.; Zabel, H.; Wolff, M. Solid surface structure affects liquid order at the polystyrene-self-assembled-monolayer interface. *Phys. Rev. E Stat. Nonlin. Soft Matter Phys.* **2013**, *87* (1), 012306. DOI: https://doi.org/10.1103/PhysRevE.87.012306.
(18) Srinivasan, U.; Houston, M. R.; Howe, R. T.; Maboudian, R. Alkyltrichlorosilane-based self-assembled monolayer films for stiction reduction in silicon micromachines. *J. Microelectromech. Syst.* **1998**, *7* (2), 252-260. DOI: https://doi.org/10.1109/84.679393.
(19) Zhang, L.; Wesley, K.; Jiang, S. Molecular Simulation Study of Alkyl Monolayers on Si(111). *Langmuir* **2001**, *17* (20), 6275-6281. DOI: https://doi.org/10.1021/la0106337.
(20) Zhan, Y.; Xing, L.; Mattice, W. L. Simulations of Self-Assembled Monolayers with the Same Surface Density but Different Grafting Patterns. *Langmuir* **1995**, *11* (6), 2103-2108. DOI: https://doi.org/10.1021/la00006a043.
(21) Barlow, D. J.; Muslim, A.-M.; Webster, J. R. P.; Penfold, J.; Hollinshead, C. M.; Jayne Lawrence, M. Molecular modelling of surfactant monolayers under constraints derived from neutron reflectance measurements. *Physical Chemistry Chemical Physics* **2000**, *2* (22), 5208-5213, 10.1039/B003437L. DOI: https://doi.org/10.1039/B003437L.
(22) Barriga, J.; Coto, B.; Fernandez, B. Molecular dynamics study of optimal packing structure of OTS self-assembled monolayers on SiO2 surfaces. *Tribol. Int.* **2007**, *40* (6), 960-966. DOI: https://doi.org/10.1016/j.triboint.2006.02.030.
(23) Craighead, H. G. Nanoelectromechanical Systems. *Science* **2000**, *290* (5496), 1532-1535. DOI: https://doi.org/10.1126/science.290.5496.1532.
(24) Chandross, M.; Webb, E. B., 3rd; Stevens, M. J.; Grest, G. S.; Garofalini, S. H. Systematic study of the effect of disorder on nanotribology of self-assembled monolayers. *Phys. Rev. Lett.* **2004**, *93* (16), 166103. DOI: https://doi.org/10.1103/PhysRevLett.93.166103.
(25) Pastorino, C.; Binder, K.; Kreer, T.; Müller, M. Static and dynamic properties of the interface between a polymer brush and a melt of identical chains. *J. Chem.*

Phys. **2006**, *124* (6), 64902. DOI: https://doi.org/10.1063/1.2162883.
(26) Li, J.; Cao, W.; Li, J.; Ma, M. Fluorination to enhance superlubricity performance between self-assembled monolayer and graphite in water. *Journal of Colloid and Interface Science* **2021**, *596*, 44-53. DOI: https://doi.org/10.1016/j.jcis.2021.03.133.
(27) Tripp, C. P.; Hair, M. L. Reaction of Methylsilanols with Hydrated Silica Surfaces: The Hydrolysis of Trichloro-, Dichloro-, and Monochloromethylsilanes and the Effects of Curing. *Langmuir* **1995**, *11* (1), 149-155. DOI: https://doi.org/10.1021/la00001a027.
(28) Virkar, A.; Mannsfeld, S.; Oh, J. H.; Toney, M. F.; Tan, Y. H.; Liu, G.-y.; Scott, J. C.; Miller, R.; Bao, Z. The Role of OTS Density on Pentacene and C60 Nucleation, Thin Film Growth, and Transistor Performance. *Adv. Funct. Mater.* **2009**, *19* (12), 1962-1970. DOI: https://doi.org/10.1002/adfm.200801727.
(29) Lepikko, S.; Jaques, Y. M.; Junaid, M.; Backholm, M.; Lahtinen, J.; Julin, J.; Jokinen, V.; Sajavaara, T.; Sammalkorpi, M.; Foster, A. S.; et al. Droplet slipperiness despite surface heterogeneity at molecular scale. *Nat. Chem.* **2024**, *16* (4), 506-513. DOI: https://doi.org/10.1038/s41557-023-01346-3.
(30) Emami, F. S.; Puddu, V.; Berry, R. J.; Varshney, V.; Patwardhan, S. V.; Perry, C. C.; Heinz, H. Force Field and a Surface Model Database for Silica to Simulate Interfacial Properties in Atomic Resolution. *Chem. Mater.* **2014**, *26* (8), 2647-2658. DOI: https://doi.org/10.1021/cm500365c.
(31) Castillo, J. M.; Klos, M.; Jacobs, K.; Horsch, M.; Hasse, H. Characterization of Alkylsilane Self-Assembled Monolayers by Molecular Simulation. *Langmuir* **2015**, *31* (9), 2630-2638. DOI: https://doi.org/10.1021/la504178g.
(32) Summers, A. Z.; Iacovella, C. R.; Cummings, P. T.; McCabe, C. Investigating Alkylsilane Monolayer Tribology at a Single-Asperity Contact with Molecular Dynamics Simulation. *Langmuir* **2017**, *33* (42), 11270-11280. DOI: https://doi.org/10.1021/acs.langmuir.7b02479.
(33) Xu, Z.; Feng, H.; Jia, Y.; Wang, J. A molecular dynamic study of the boiling heat transfer on a liquid metal surface with different thicknesses. *Case. Stud. Therm. Eng.* **2024**, *64*. DOI: 10.1016/j.csite.2024.105505.
(34) Shiga, M.; Morishita, T.; Aichi, M.; Nishiyama, N.; Sorai, M. Correlation between Contact Angle and Water Film Energetics in Carbon Dioxide–Water–Clay Mineral Interfacial Systems: A Molecular Dynamics Study. *Energy Fuels* **2023**, *37* (21), 16688-16700. DOI: 10.1021/acs.energyfuels.3c02471.
(35) Jorgensen, W. L.; Maxwell, D. S.; Tirado-Rives, J. Development and Testing of the OPLS All-Atom Force Field on Conformational Energetics and Properties of Organic Liquids. *Journal of the American Chemical Society* **1996**, *118* (45), 11225-11236. DOI: https://doi.org/10.1021/ja9621760.
(36) Thompson, A. P.; Aktulga, H. M.; Berger, R.; Bolintineanu, D. S.; Brown, W. M.; Crozier, P. S.; in 't Veld, P. J.; Kohlmeyer, A.; Moore, S. G.; Nguyen, T. D.; et al. LAMMPS - a flexible simulation tool for particle-based materials modeling at the atomic, meso, and continuum scales. *Comput. Phys. Commun.* **2022**, *271*, 108171. DOI: https://doi.org/10.1016/j.cpc.2021.108171.

(37) Frenkel, D.; Smit, B. Chapter 6 - Molecular Dynamics in Various Ensembles. In *Understanding Molecular Simulation (Second Edition)*, Frenkel, D., Smit, B. Eds.; Academic Press, 2002; pp 139-163.
(38) Wang, M.; Liechti, K. M.; Srinivasan, V.; White, J. M.; Rossky, P. J.; Stone, M. T. A Hybrid Continuum-Molecular Analysis of Interfacial Force Microscope Experiments on a Self-Assembled Monolayer. *Journal of Applied Mechanics* **2004**, *73* (5), 769-777. DOI: https://doi.org/10.1115/1.1943435.
(39) Allara, D. L.; Parikh, A. N.; Rondelez, F. Evidence for a Unique Chain Organization in Long Chain Silane Monolayers Deposited on Two Widely Different Solid Substrates. *Langmuir* **1995**, *11* (7), 2357-2360. DOI: https://doi.org/10.1021/la00007a007.
(40) Kumar, V.; Dhillon, A. S.; Sharma, N. N. Surface Modification of Textured Dielectrics and Their Wetting Behavior. *J. Mater. Eng. Perform.* **2017**, *26* (2), 822-827. DOI: https://doi.org/10.1007/s11665-017-2505-1.
(41) Kong, Z.; Wang, Q.; Chen, E.; Wu, T. Study on preparation method for short-chain alkylsiloxane self-assembled monolayers and the diffusion behavior of copper on silica surfaces. *Appl. Surf. Sci.* **2013**, *279*, 171-179. DOI: https://doi.org/10.1016/j.apsusc.2013.04.064.
(42) Xia, F.; Jiang, L. Bio-Inspired, Smart, Multiscale Interfacial Materials. *Adv. Mater.* **2008**, *20* (15), 2842-2858. DOI: https://doi.org/10.1002/adma.200800836.
(43) Zhang, D.; Ji, J.; Yan, C.; Zhang, J.; An, Z.; Shen, Y. Research advances in bio-inspired superhydrophobic surface: Bridging nature to practical applications. *J. Ind. Eng. Chem.* **2024**, *140*, 20-46. DOI: https://doi.org/10.1016/j.jiec.2024.05.051.
(44) Wenzel, R. N. RESISTANCE OF SOLID SURFACES TO WETTING BY WATER. *Ind. Eng. Chem.* **1936**, *28* (8), 988-994. DOI: https://doi.org/10.1021/ie50320a024.
(45) Cassie, A. B. D.; Baxter, S. Wettability of porous surfaces. *Trans. Faraday Society* **1944**, *40* (0), 546-551, 10.1039/TF9444000546. DOI: https://doi.org/10.1039/TF9444000546.
(46) Zhang, Y.; Chen, Y.; Shi, L.; Li, J.; Guo, Z. Recent progress of double-structural and functional materials with special wettability. *J. Mater. Chem.* **2012**, *22* (3), 799-815, 10.1039/C1JM14327A. DOI: https://doi.org/10.1039/C1JM14327A.
(47) Chu, F.; Lin, Y.; Yan, X.; Wu, X. Quantitative relations between droplet jumping and anti-frosting effect on superhydrophobic surfaces. *Energy and Buildings* **2020**, *225*, 110315. DOI: https://doi.org/10.1016/j.enbuild.2020.110315.

Table of Contents graphic

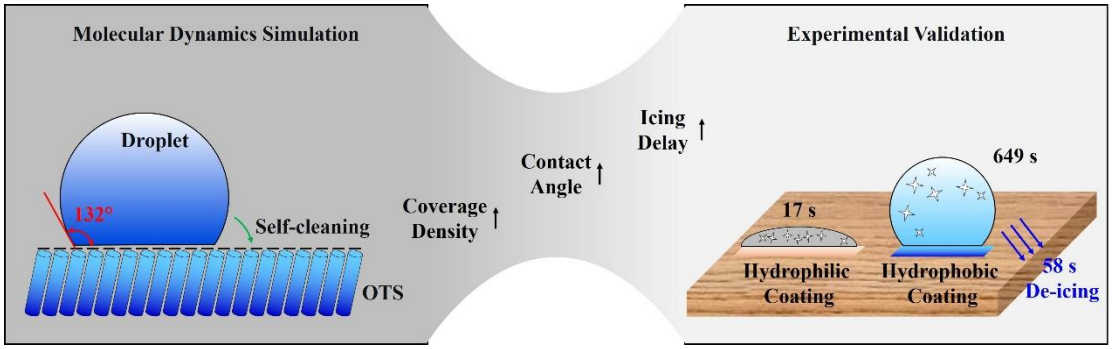

For Table of Contents Use Only